Journal Pre-proof

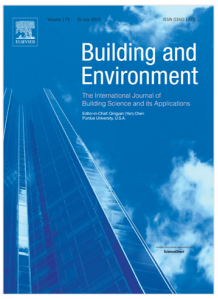

On the effects of walking speed, crowd density and human-to-source distance on pollutant dispersion in indoor spaces

H.D. Lim, Timothy G. Foat, Simon T. Parker, Christina Vanderwel

PII: S0360-1323(24)00491-8
DOI: https://doi.org/10.1016/j.buildenv.2024.111649
Reference: BAE 111649

To appear in: *Building and Environment*

Received date : 4 March 2024
Revised date : 24 April 2024
Accepted date : 14 May 2024

Please cite this article as: H.D. Lim, T.G. Foat, S.T. Parker et al., On the effects of walking speed, crowd density and human-to-source distance on pollutant dispersion in indoor spaces, *Building and Environment* (2024), doi: https://doi.org/10.1016/j.buildenv.2024.111649.

Available online at www.sciencedirect.com

ScienceDirect

Building & Environment 00 (2024) 1–19

Building & Environment

On the effects of walking speed, crowd density and human-to-source distance on pollutant dispersion in indoor spaces

H.D. Lim[a], Timothy G. Foat[b,c], Simon T. Parker[b], Christina Vanderwel[c,]

[a]School of Civil, Aerospace and Design Engineering, University of Bristol, BS8 1TR, United Kingdom
[b]Defence Science and Technology Laboratory, Salisbury, United Kingdom
[c]Department of Aeronautical and Astronautical Engineering, University of Southampton, SO16 7QF, United Kingdom

Abstract

The effects of walking speed, crowd density and human-to-source distance on pollutant dispersion in two scaled room models are investigated using simultaneous planar laser-induced fluorescence and particle-image velocimetry techniques. For a small 3 m high room, where the length-scales of the people and room are comparable, the walking motions significantly influenced the macro room mean flow patterns. This has a strong effect on the scalar dispersion properties as the magnitudes of the advective scalar fluxes are often comparable or larger than the turbulent scalar fluxes. As such, the scalar dispersion properties are case specific. For a large 9 m high room, the walking motion influenced only the local mean flow field. The increase in walking speed and crowd density improves the efficiency in which the scalar is transported and mixed with fresh ambient fluid out of the measurement plane (i.e. along the direction of the motion), leading to scalar-free zones observed on the opposite side of the room from the ventilation outlet. The area of the scalar-free zone increases with an increase in the walking speed and crowd density. The advective scalar fluxes are more sensitive to the human motion than the turbulent components, and as the mixing efficiency improves, the advective fluxes show a greater weakening with increased distance from source. The concentration PDFs in the near-source region can be described by the exponential function where the expected value at the 99% percentile can be derived as C_{99}/c'_{rms}=4.61, which agreed well with the experimental measurements of 4.1 to 5.9.

Keywords: Indoor airflow, crowd effects, scalar dispersion, indoor air quality, risk assessment

1. Introduction

Understanding scalar dispersion in indoor spaces is an essential aspect of improving public health and well-being, as there are many infectious viral and bacterial diseases that can be transmitted through the airborne route. This includes the SARS-CoV-2 virus which is responsible for the COVID-19 pandemic, the common cold and influenza, tuberculosis and chickenpox. A recent multidisciplinary review has presented strong evidence of the association between indoor airflow and the transmission of airborne diseases [1] which highlights the importance of, and the need to, better understand indoor airflows.

Indoor airflow is complex due to the lack of clearly defined air flow paths and its sensitivity to a wide range of different parameters. In the absence of strong pressure variations (i.e. naturally ventilated empty rooms), thermal stratification tends to determine the flow patterns, with the three main forms of stratification being: 'stable stratification', 'unstable stratification' and the 'gravity current' [2]. For mechanically ventilated rooms, the air changes per

Email address: c.m.vanderwel@soton.ac.uk (Christina Vanderwel)

hour (ACH) is a particularly important parameter, and its strong influence on scalar mixing and indoor air quality is widely recognised [3, 4, 5]. There are many other parameters that can influence indoor airflow and air quality. Recent studies have examined the effects of the relative position of inlet and outlet vents in convective flows [6], the effects of temperature and relative humidity on exposures to airborne pathogens [7], the seasonal variations in carbon dioxide levels in 36 naturally ventilated classrooms in the UK monitored throughout 2021 [8], and the impact of human movements on particle dispersion and resuspension [9].

In scenarios where hazardous air pollutants are released in crowded indoor spaces, which can include airborne pathogens or toxic chemical gases, our understanding of scalar dispersion is crucial to support accurate assessments of exposures and pre-planned decisions that can mitigate the consequences and save lives. These decisions can be in the form of official instructions for people to evacuate from the incident site or to seek shelter [10]. The effects of human activities may have a significant influence on the dispersion and concentrations of the pollutants, and is therefore, an important factor that needs to be considered to better inform decisions and to avoid unintended effects.

There have been several studies focusing on the effects of walking on scalar dispersion. Wang & Chow [11] numerically studied the effects of walking motion on expiratory droplets, and observed that higher walking speeds reduce the overall amount of suspended droplets by increasing the removal rate of pollutants through the ventilation outlet. Tan et al. [12] observed higher walking speeds of medical staff led to more significant secondary airflow and therefore, lower number of particles settling on a patient in an isolation ward. Mingotti et al. [13] experimentally investigated the repeated passage of a person along a corridor and focused on the effects of the wake-driven mixing on the turbulent diffusivity, which is a parameter that describes the rate of turbulent scalar mixing. Empirical observations suggest the turbulent diffusivity coefficient is a function of the characteristic length-scales of the corridor and the person, as well as the average frequency of the person moving along the corridor.

The impact of walking on scalar dispersion are often considered in the context of other key parameters, such as the room airflow patterns or the proximity to the inlet/outlet/region of interest. Hang et al. [14] investigated the effects of ACH, ventilation design, and walking motion of realistic vs idealised (rectangular block) body geometries. Their results showed the effects of ventilation design can be more significant in influencing gaseous pollutant spread than the human motion. Lv et al. [15] observed that different human walking patterns can lead to complex interactions between the thermal plume from a kitchen hob and the wake flow generated by the walking motion. Al Assaad et al. [16] simulated a static and a moving thermal manikin model, and showed the turbulence produced by a moving model can create local mixing effects, which enhanced the entrainment of contaminants from the room into a personalised ventilation jet. Liu et al. [17] performed Reynolds-averaged Navier-Stokes (RANS) simulation on a circulating nurse walking in an operating room to study its effect on the airflow and pollutant concentration. Although higher pollutant concentration was observed near the instrument tables, the airflow above the operating table which was slightly further from the circulating nurse was not affected, thus indicating that the walking-induced turbulence and mixing effects are localised.

The airflow is much more complex in crowd scenarios but has many important applications particularly in public spaces such as transport platforms. Zhao et al. [18] performed simulations to investigate the effects of human movements on droplet and aerosol transport in an airport terminal. When the walking direction is perpendicular to the room flow, the effect of the crosswind led to increased droplet dispersion perpendicular to the walking direction, as compared to the perpendicular dispersion when walking into or against the room flow. Marlow et al. [19] used a multidisciplinary simulation tool based on the lattice-Boltzmann method, a wake model and a human agent behavioral model to simulate an evacuation scenario. They observed higher concentrations of air pollutants near the room exit, due to pollutant entrainment by the wake flow of people leaving the room. Wu et al. [20] observed a much more extensive pollutant dispersion range in the multi-person walking configuration (as compared to the single-person), for aerosols and droplets exhaled by a moving person in the middle of the room.

Besides walking, there are several studies that have looked into the effects of other human-related factors on indoor scalar dispersion. For example, Hathway et al. [21] investigated the effects of door motion on mass exchange between two rooms and observed large-scale vortex and jet-like motions governing the transport and mixing processes, and a linear relationship between door hold-open time and volume flux between the two rooms. Kamar et al. [22] investigated turning movements of medical staff in an operating room. A bent forearm was observed to change the flow field more significantly than a straight forearm and increased the concentrations of particle settling on the patient. Abouelhamd et al. [23] investigated the effect of crowd density on the human breathing zone for social distancing applications. As the crowd density decreases from 3 people occupying one square meter (ppl m^{-2}) to 0.25 ppl m^{-2},

the horizontal propagation of the breathing zone can increase by up to three-fold.

To better understand the current trends of indoor airflow research, here, we discuss key takeaways from selected review articles [24, 25, 9]. The advancements in the fundamental understanding of indoor airflow in the past few decades have mainly focused on relatively idealistic room geometries [24, 25]. For realistic room flows, the occupied regions of the room tend to have weak forced advection [26], which can lead to Reynolds number (Re) dependent flow in some regions of the room despite the flow at the ventilation inlet having already achieved Re independence [27]. The complexity of indoor room flow is well documented and different flow dynamics (such as jet flows, recirculation zones, laminar or fully turbulent flows) can exist in different regions of the room simultaneously [26, 28, 25]. As a result, it can be challenging for Computational Fluid Dynamics (CFD) methods to model the problem. Kek et al. [9] recently reviewed human movements in indoor airflow literature, and found RANS and URANS simulations are still the most popular methods in indoor airflow studies involving either static or dynamic people. Many studies apply the dynamic meshing technique to account for human movements, and treat the humans as the pollutant source (i.e. either as a direct source of aerosols/droplets and/or an indirect source due to particle resuspension). Despite the popularity of CFD approaches, experimental results are still considered vital as a validation dataset due to the complexity of the airflow in a room. Nonetheless, accurate experimental results from full-scaled chamber could be challenging to collect in dynamic airflow measurements, as human intrusion during the measurements would introduce uncertainties [9].

The research objective of this study is to investigate the effects of walking speed, crowd density and human-to-source distance on the full-field concentration statistics and scalar transport mechanisms of pollutants from a point-source in two scaled indoor spaces (i.e. a small 3 m ceiling room and a large 9 m ceiling room). Simultaneous particle-image velocimetry (PIV) and planar laser-induced fluorescence (PLIF) experiments on two scaled room models were performed, which enabled access to completely non-intrusive and full-field concentration and velocity measurements. To the best of the authors' knowledge, there are currently very limited studies with a similar research objective, and this may be one of the very first experimental studies that offers a unique perspective on the full-field concentration statistics (which include the peak-to-mean concentration and concentration probability density functions (PDFs)) and the covariance of the concentration and velocity (i.e. turbulent scalar fluxes). As high-fidelity experimental dataset are scarce, we hope that our open access dataset will be beneficial to the indoor airflow community.

In section 2, we present the description of our experimental setup and test parameters. Section 3 discusses the effects of walking speed, crowd density and human-to-source distance on the concentration statistics. In section 4, we discuss the concentration-velocity statistics and the scalar transport mechanisms. Section 5 presents the key conclusions of our study.

2. Experimental methodology

2.1. Setup and data acquisition

The experiments were performed in the University of Southampton's Boldrewood Campus Recirculating Water Tunnel (flume) facility. A schematic of the experimental setup is shown in figure 1(a). The room model was installed in an upside-down configuration to enable the mechanical traverse system to actuate the cylinder models, which represent people, from the top of the flume. The room model was fully submerged, spanned across the entire width of the flume (W = 1200 mm), and flow was driven by the flume's pumps through a channel of height $h_{channel}$ = 40 mm. After the inlet channel, the flow entered the room model through 6×2 h_{inlet} = 60 mm diameter round ventilation inlets with 80 mm diameter round deflector plates. The ventilation inlets were spaced at 180 mm from each other as shown in figure 1(b). The flow exited the room through a one-sided ground level opening (with height h_{exit}), which is representation of an open doorway as shown in figure 1(c). The motivation and design of the room geometry can be found in an earlier study [29] which readers can refer to for more details.

Figure 1(c) shows the key dimensions of the room model, which was machined entirely out of clear acrylic to allow optical access, and covered with matt black vinyl tape to reduce laser reflections. The design and key dimensions of the ventilation inlet are shown in figure 1(b), which was also machined using clear acrylic. An image of the partially assembled room is shown in figure 2(a), where the top plate (i.e., room floor) was lifted to show the ventilation inlet. We investigated two different room designs in the experiments. Room A is a 20:1 full-to-model scale room that has $h_{exit,A}$=100 mm and represents a 3 m ceiling room that is typical of small offices or houses. Cylinders in room A

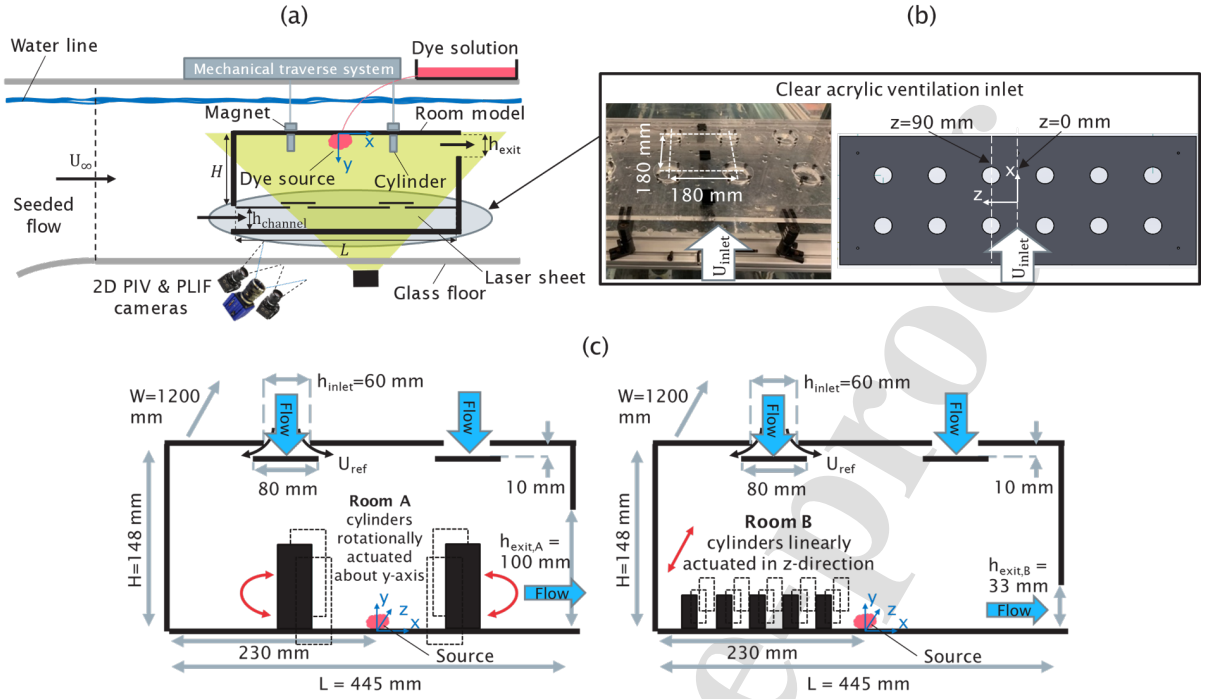

Figure 1. Schematic of (a) the experimental setup with room model in an upside down configuration, (b) the ventilation inlet grid and (c) key dimensions of room A (left) and room B (right).

which were used as a proxy for people have a height of 75 mm and diameter of D_A=25 mm. Room B is a 60:1 full-to-model scale room that has $h_{exit,B}$=33 mm and represents a 9 m ceiling room that is typical of bigger rooms such as an auditorium or a lecture hall. Cylinders in room B have a height of 25 mm and diameter of D_B=8 mm.

The patterns of people's movement in indoor spaces are linked to behavioral patterns and would therefore be dependent on specific applications. Valid motions can range from static, if people are resting, to random directional motion, or the convergence of people at a common location in an evacuation scenario. Complex behaviour can also emerge, such as lane formation in the flows of people in opposing directions [30]. In this study, complex behaviour patterns are not taken into account, due to the complexity of the experimental setup, with people's movement simplified into two main types of motion.

Room B cylinder arrays (figures 2(d,f)) were linearly actuated using the flume's linear z-direction mechanical traverse system as shown in figures 1(c) and 2(b). Their movement was prescribed with a triangular displacement-time waveform with peak-to-peak amplitude of 160 mm (i.e. $20D_B$) for all test cases in this study. Room B cylinder arrays occupy only one side of the room, on the opposite side of the room to the outlet, as shown in the schematic in figure 1(c). This is of interest as it represents a realistic dilemma where a decision has to be made on whether people should evacuate through the scalar source to the exit on the other side of the room, or to seek shelter on their side of the room. Note that the side of the room closer to the exit is empty as we have assumed people close to the room outlet would always choose to evacuate.

Room A cylinder pairs (figures 2(d,e)) were actuated with a stepper motor to achieve rotational motion about the y-axis of the point source as shown in figures 1(a) and 2(c). This was prescribed a triangular angular displacement-time waveform with peak-to-peak amplitudes of 60°, 20° and 19.2° at constant cylinder-to-source distances of $2D_A$, $4D_A$ and $6D_A$ respectively. All of these correspond to a peak displacement of 50 mm in the z-direction. In the rotational motion case, the positions of the two cylinders are always equidistant from the scalar source in the x-direction.

The cylinders in the room model cannot be actuated by machining holes in the top plate (room floor) as it would lead to tracer dye escaping the room. To circumvent this problem, two strong round neodymium magnets were

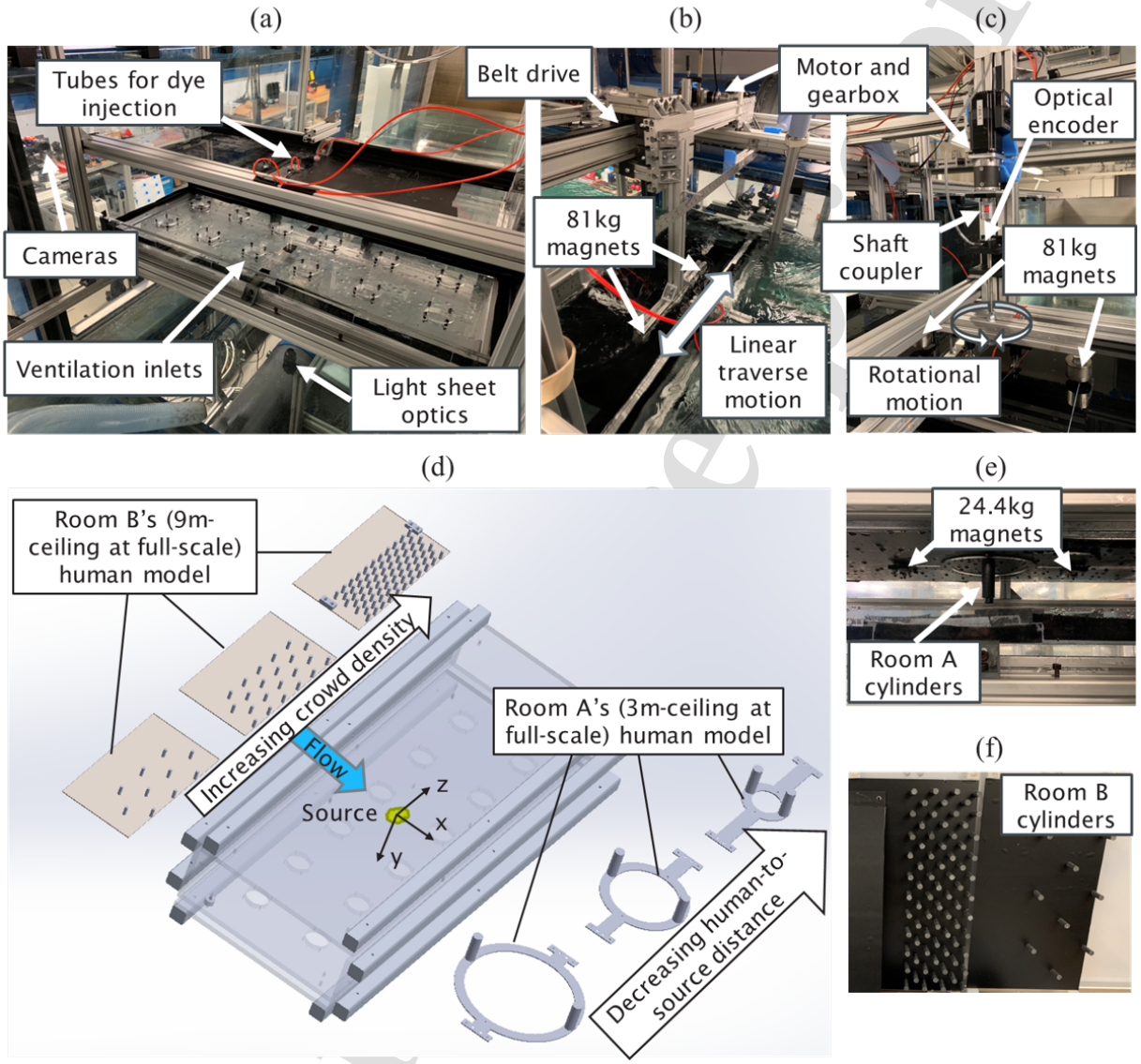

Figure 2. (a) Partial assembly of the room setup in the upside down configuration, (b) linear traverse for room B cylinder motions, (c) rotational setup for room A cylinder motions, (d) schematic of test models, (e) room A cylinders in upside down configuration held by magnets and (f) the construction of room B cylinder array.

mounted on the traverse system (this is visible in figure 2(c), each magnet is capable of pulling 81 kg) which attracted two smaller rectangular (40 mm × 20 mm × 10 mm) neodymium magnets (each capable of pulling 24.4 kg) mounted onto thin (up to 3 mm) sheets on which the cylinders were attached. The use of very strong magnets is necessary due to the spatial separation (i.e. air gap) between the magnets. To avoid clamping the cylinder model to the room floor, two ball transfer units were used to support the round magnets on the traverse system, and four miniature ball transfer units were used to support the plates on which the cylinders were mounted. This also helped to reduce friction between the cylinder plate and the room floor. Figure 2(e) shows room A cylinder model held in place by the magnets and figure 2(f) shows the construction of room B cylinder arrays, where the cylinders were machined out of nylon rods and screwed onto the 3 mm thin, 400 mm × 200 mm acrylic sheets (i.e. cylinder plate). Room A cylinders were constructed in a similar manner, but with a different cylinder plate design, as shown in figures 2(d,e).

The concentration and velocity statistics were measured simultaneously in the xy-plane at z=0 (see figure 1) using PLIF and PIV techniques. For PLIF, Rhodamine 6G fluorescent dye which has a Schmidt number of Sc=2500±300 [31] was used as a passive scalar tracer and released at the origin via a 2.5 mm inner diameter tube. The source concentration was C_s=10 mg L^{-1} for all test cases. The dye flow rate of Q_{dye}=10 mL min^{-1} was maintained using a needle valve and a Mariotte's bottle reservoir. As the dye flow rate is very low, the dye equilibrates rapidly with the room flow and would therefore not have any influence on the scalar dispersion properties [32]. The choice of our scalar tracer meant that our findings are applicable to gaseous pollutants and very fine particulate matter where the particle velocity response time (which is a function of the particle density and diameter) is low. The effects of pollutant resuspension or dry deposition are not considered in this study. For PIV, 50 μm polyamide seeding particles were recirculated in the flume until uniform seeding was achieved. The water quality was closely monitored and treated to ensure any changes to the background levels of Rhodamine 6G dye, agglomeration of seeding particles or bio-fouling did not contribute to experimental uncertainties. A Nd:YAG double-pulsed laser (emission wavelength of 532 nm) and laser optics were used to form a laser sheet to illuminate the seeding particles and excite the fluorescent dye which fluoresce at 554 nm. To separate the signals from the seeding particles and fluorescent dye, a 540 nm long-pass filter was fitted to the PLIF camera (5.4 MP 16-bit depth Imager sCMOS) and 532 nm laser-line bandpass filters were fitted to the PIV cameras (two 4 MP Imager MX CMOS cameras in side-by-side configuration). For all test cases, 1000 realisations of the flow field were captured at an acquisition frequency of either 2 Hz or 2.5 Hz. This is dependent on the exact test cases as the dataset presented in this study came from multiple experimental campaigns and has negligible effects on the results and discussions in this study.

The image post-processing procedures are similar to several of our recent studies which readers can refer to for more details [32]. The particle images were post-processed using LaVision DaVis 10 software. Image pre-processing was performed to remove background noise before performing multi-pass, multi-grid cross-correlation analysis with an overlap ratio of 50%. Spurious vectors were removed and replaced using local neighbourhood standard deviation and median filters. The final vector resolution is 1.56 mm. A conservative estimate of the velocity bias is 0.5% and the standard error of the mean statistics estimated based on the standard bootstrap with replacement statistical procedure is 3% at 95% confidence interval. The PLIF post-processing was implemented using an inhouse code where PLIF images were calibrated against the background, 0.03 mg L^{-1} and 0.05 mg L^{-1} concentrations of dye in two calibration tanks, to obtain the linear relationship between the fluorescence intensity and dye concentration. Light attenuation in the calibration tanks was accounted for using the Beer-Lambert's law and temporal variations in the laser pulses were accounted for using an energy monitor device attached to the laser. The PLIF resolution is 0.174 mm. A conservative estimate of the bias error is 10.2% at 95% confidence interval and the standard error is estimated to be 1% based on the bootstrap with replacement statistical procedure. An image masking procedure was performed for regions where the field-of-view was obstructed, and consequently, these regions are not considered in the discussions.

2.2. Test parameters

The test parameters investigated in this study are presented in table 1. The first group of eight rows presents the test parameters used to investigate the effects of walking speed for rooms A and B, characterised by the Reynolds number based on the diameter and mean velocity of the cylinders. The dynamic similarity of the walking motion was matched using Re_{crowd}, which was calculated based on the diameters of the cylinders and their walking speed (U_{crowd}). The Re_{crowd} investigated in this study are lower than that of a full-scale human walking which is approximately $Re \approx 20,000$, but the cylinder flow regimes are the same (subcritical regime with fully turbulent vortex streets [33]) hence results and trends are expected to be representative. The next group of four rows (separated by the black line)

Table 1. Test parameters for rooms A (20:1) and B (60:1). The subscript 'FS' denotes full-scale quantities where applicable. Test cases with repeated entries are marked by superscripts * and #.

Test case	U_{ref} [m s^{-1}]	$U_{ref,FS}$ [m s^{-1}]	Re_{inlet}	ACH_{FS} [h^{-1}]	U_{crowd} [m s^{-1}]	$U_{crowd,FS}$ [m s^{-1}]	Re_{crowd}	Crowd density [ppl m^{-2}]	Human-to-source distance (D)
B-WS0	0.29	0.07	17,400	1.9	0	0	0	0.125	4.3
B-WS1	0.29	0.07	17,400	1.9	0.10	0.03	768	0.125	4.3
B-WS2	0.29	0.07	17,400	1.9	0.19	0.05	1536	0.125	4.3
B-WS3*	0.29	0.07	17,400	1.9	0.32	0.08	2560	0.125	4.3
A-WS0	0.19	0.14	11,200	10.8	0	0	0	-	4
A-WS1	0.19	0.14	11,200	10.8	0.08	0.06	2000	-	4
A-WS2#	0.19	0.14	11,200	10.8	0.16	0.12	4000	-	4
A-WS3	0.19	0.14	11,200	10.8	0.22	0.17	5500	-	4
B-CD0	0.29	0.07	17,400	1.9	0.32	0.08	2560	0	4.3
B-CD1	0.29	0.07	17,400	1.9	0.32	0.08	2560	0.05	4.3
B-CD2*	0.29	0.07	17,400	1.9	0.32	0.08	2560	0.125	4.3
B-CD3	0.29	0.07	17,400	1.9	0.32	0.08	2560	0.5	4.3
A-HS1	0.19	0.14	11,200	10.8	0.16	0.12	4000	-	2
A-HS2#	0.19	0.14	11,200	10.8	0.16	0.12	4000	-	4
A-HS3	0.19	0.14	11,200	10.8	0.16	0.12	4000	-	6

presents the test parameters used to investigate the effects of crowd density, and is characterised by the number of people occupying one square meter (ppl/m^2) at full-scale. The last group of three rows presents the test parameters used to investigate the effects of human-to-source distance. The human-to-source distance is measured from the center of the cylinders in the row that is closest to the source. Some of the test cases are repeated in different groups, and are organised in this manner to allow readers to easily compare the test parameters of specific crowd effects.

The dynamic similarity of the room flow to the full-scale problem is achieved by matching the Reynolds number (Re_{inlet}) based on U_{ref} and h_{inlet} [34], which represents the characteristic velocity and length scales associated with the ventilation inlet respectively. Note that U_{ref} is in effect the spatially-averaged flow velocity at the inlet, as it was calculated using the room flow rate and the inlet area, where the room flow rate was estimated using velocity profiles measured at the outlet for z=0 and z=90 mm planes. Our Re_{inlet} is similar to some [35, 29] and higher than other studies [34, 26]. The ventilation time scale was calculated using the room volume and room flow rate (i.e. $1/ACH \times 3600$), which led to full-to-model ventilation time scale ratios of t_{ratio}=26.7 for room A (geometric scale ratio, L_{ratio}=20) and t_{ratio}=240 for room B (geometric scale ratio, L_{ratio}=60). Using these ratios, full-scale parameters can be calculated (denoted by subscript 'FS' in this study) [29]. An example equation to convert the model-scale U_{ref} to full-scale is given by:

$$U_{ref,FS} = U_{ref} \times \frac{L_{ratio}}{t_{ratio}}. \quad (1)$$

The same methodology was used to calculate the ACH_{FS}, which in this study (table 1), are comparable to several past studies and representative of indoor spaces [36, 3].

3. Concentration statistics

In this section, we examine the effects of the walking speed, crowd density and human-to-source distance on the concentration statistics, which may be useful to inform guidelines for incidents where hazardous air pollutants are accidentally released in indoor spaces. As the movement of the cylinder models for room A and B were not synchronised with the PLIF-PIV imaging system, our analysis will only focus on the statistics of the xy-plane at z=0 and the effect of the full period of motion in our analysis (instead of examining the flow field at different phases of the

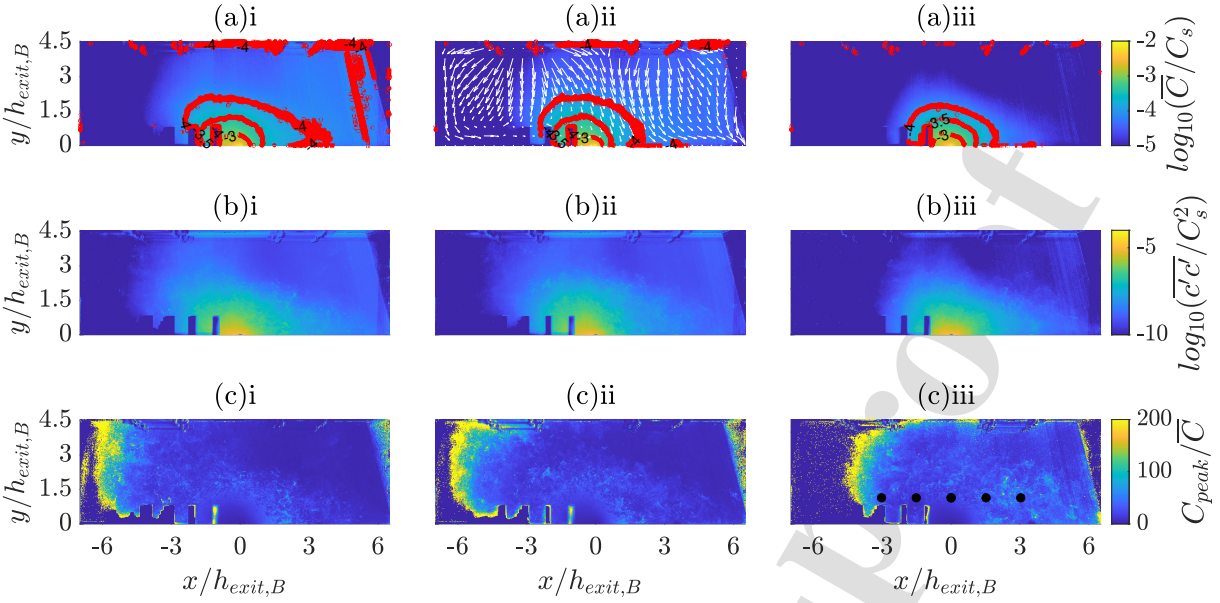

Figure 3. Effects of walking speed, room B. (a) Mean concentration, (b) concentration variance and (c) peak-to-mean concentrations for test cases (i) B-WS0, (ii) B-WS1 and (iii) B-WS3 (i → iii: increasing walking speed). The white arrows represent mean velocity vectors, red represents isocontour lines of the mean concentration and black dots represent the locations where the concentration PDF is extracted.

cylinder motion). In this study, $\overline{C}$ and c' represent the time-averaged (mean) concentration and instantaneous concentration fluctuation respectively. C_{peak} represents the maximum concentration measured over the entire experimental acquisition time.

3.1. *Effects of walking speed*

Figure 3 shows the concentration statistics for room B. The mean velocity vectors are overlaid for only the B-WS1 test case in figure 3a(ii) as they are similar across the three test cases. The similarity of the flow field across the test cases can be attributed to the relatively small length-scales of the cylinders compared to the room, hence differences in their walking speed did not significantly affect the room flow at the macro scale.

With an increase in walking speed (i.e. figure 3i → 3iii), lower magnitudes of mean concentrations are observed at regions far from the source. The isocontour lines at the near-source region take on a more uniform hemispherical shape (figure 3a(iii)) and in particular, closer isocontour lines to the right of the source show an increase in the magnitude of the mean concentration gradient particularly towards the room outlet. The magnitudes of the concentration variance are highest at the source and decay with distance from source. The variance magnitudes are observed to decay more quickly as the walking speed increases (i.e. figure 3(b)i → 3(b)iii), particularly in the left side of the room, which is occupied by the cylinders.

The trends observed here offer insights to the scalar mixing in the out-of-plane z-direction and the in-plane xy-direction, as they have competing effects on the mean concentration and concentration variance of the xy-plane at z=0 as presented in figure 3. As an example, if there is infinitely efficient scalar mixing in the out-of-plane z-direction, and negligible scalar mixing in the in-plane xy-direction, then we can expect negligible mean concentration and concentration variance maps in the xy-plane at z=0. This is because the scalar is transported out of the xy-plane much quicker than it is allowed to mix in the in-plane direction. Similarly, with an infinitely efficient scalar mixing in the in-plane xy-direction, and negligible scalar mixing in the out-of-plane z-direction, we would expect the mean concentration maps for xy-plane at z=0 to show uniform magnitudes in the entire room.

Since the increase in walking speed led to lower magnitudes of the mean concentration and concentration variance as shown in figure 3, this is indicative that there is much more significant improvement of the scalar mixing in the out-of-plane z-direction, which is aligned with the direction of the human motion, than in the in-plane xy-direction (i.e.

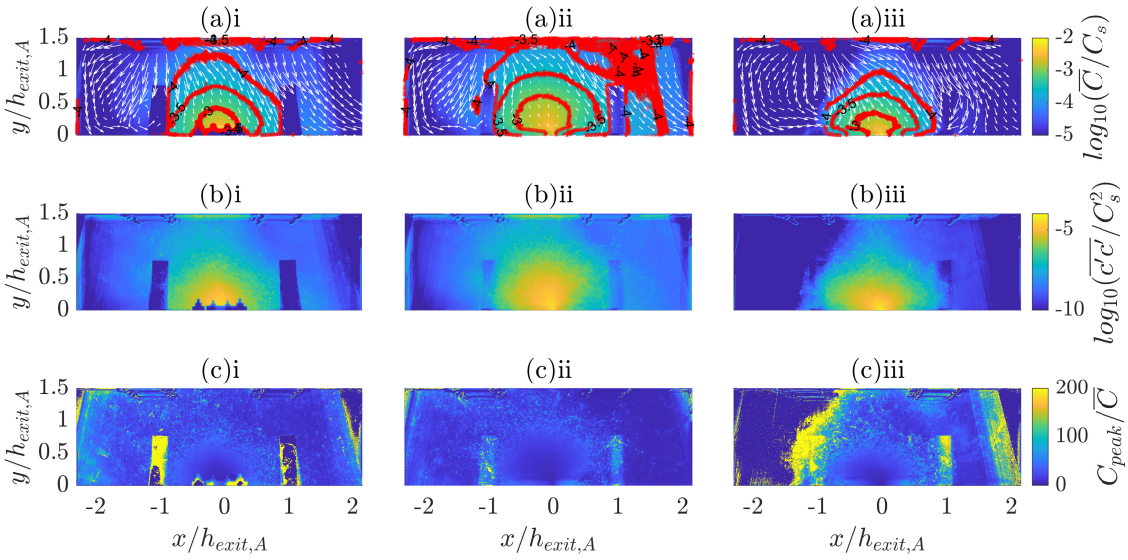

Figure 4. Effects of walking speed, room A. (a) Mean concentration, (b) concentration variance and (c) peak-to-mean concentrations for test cases (i) A-WS0 baseline, (ii) A-WS1 and (iii) A-WS3 (i → iii: increasing walking speed). The white arrows represent mean velocity vectors and red represents isocontour lines of the mean concentration.

scalar mixing is non-uniform and anisotropic). This observation is consistent with the literature, where Marlow et al. [19], Mingotti et al. [13] and Hang et al. [14] have all observed pollutant entrainment due to the wake flow of people, and in particular, Marlow et al. [19] observed higher concentrations of air pollutants close to where people cluster together. Therefore, the improvement in scalar mixing in the z-direction is likely due to the z-direction movements of the cylinder arrays in room B.

In the context of assessing exposures to toxic chemicals with high toxic load exponents [37, 38], insight into short-duration events is needed. The peak-to-mean concentration ratio ($C_{peak}/\overline{C}$) is a useful parameter that represents the maximum concentration relative to the time-averaged (i.e. mean) concentration measured in the entire acquisition time. The $C_{peak}/\overline{C}$ maps are presented in figure 3(c), where large magnitudes are observed in the left side of the room occupied by the cylinders. Intriguingly, the magnitude peaks are always connected to the cylinder array, and as the walking speed increases, they shift towards rows of cylinders that are closer to the source. Even further to the left, the row of cylinders furthest from the source appear to be in a scalar-free zone, which is defined as any region where negligible magnitudes of mean concentrations and $C_{peak}/\overline{C}$ are observed. We will return to this interesting flow feature and discuss it in greater detail in section 3.4.

The effects of walking speed for room A are examined with the mean concentration statistics presented in figure 4. With an increase in walking speed, the mean velocity vector maps show slightly different flow fields for each of the test cases, indicating the motion of the cylinders has an influence on the room flow. This is likely due to the comparable length-scales of the cylinders and the room, which was not the case in the results shown for room B. The mean concentration isocontour lines are relatively symmetrical about the source as compared to the previous room B configuration, likely due to the symmetric cylinder positions. Similar to room B, the increase in walking speed led to lower magnitudes of mean concentration and concentration variances in regions far from the source, particularly in the left side of the room, as shown in figures 4(a)iii and 4(b)iii. The $C_{peak}/\overline{C}$ ratio is presented in figure 4(c). High magnitudes of the $C_{peak}/\overline{C}$ ratio are observed only for the A-WS3 test case. This is likely because the rotational motion of the left cylinder (about the vertical y-axis) has improved scalar mixing and transport of the scalar out of the xy-plane much more significantly than the scalar transport and mixing within the xy-plane. As such, the magnitudes of the mean concentration as shown in figure 4(a)iii are low, which is a necessary condition for high magnitudes of the $C_{peak}/\overline{C}$ ratio. We will return to discuss the $C_{peak}/\overline{C}$ parameter in greater detail by examining the concentration

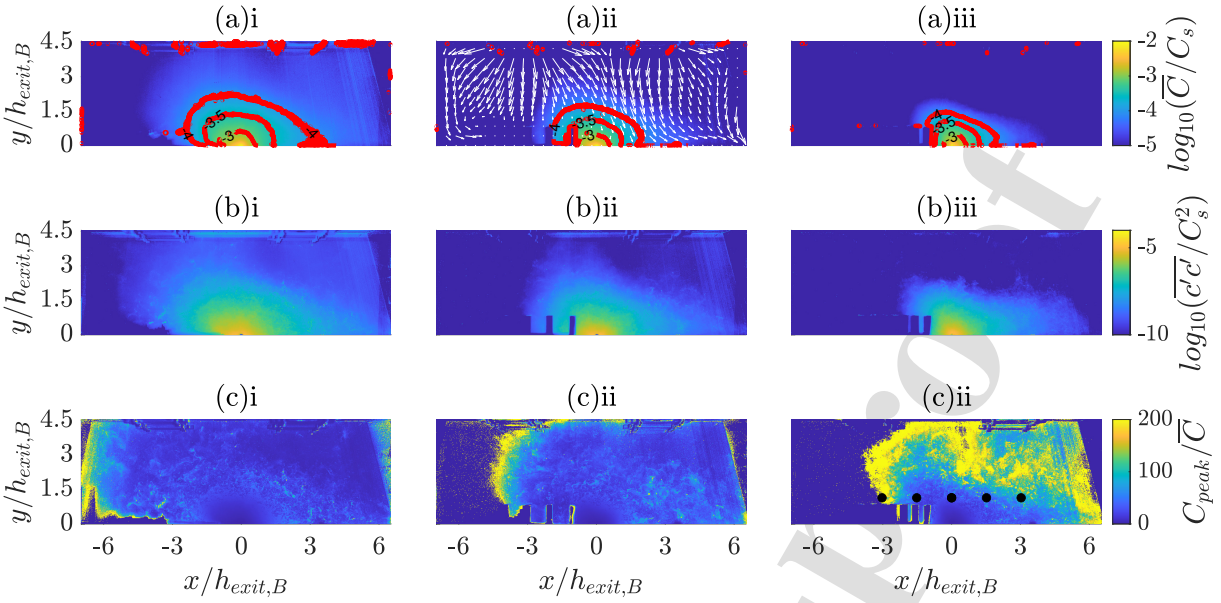

Figure 5. Effects of crowd density, room B. (a) Mean concentration, (b) concentration variance and (c) peak-to-mean concentrations for test cases (i) B-CD0, (ii) B-CD2 and (iii) B-CD3 (i → iii: increasing crowd density). The white arrows represent mean velocity vectors, red represents isocontour lines of the mean concentration and black dots represent the locations where the concentration PDF is extracted.

PDFs in section 3.4.

3.2. *Effects of crowd density*

The effects of crowd density for room B are presented in figure 5, where mean velocity vectors are shown in only one test case as they are similar across all three test cases. With an increase in the crowd density, the shape of the mean concentration isocontour lines remain similar, but the magnitudes of the mean concentration decay more rapidly with distance from source, thus indicating more efficient out-of-plane scalar mixing in the near-source region. The concentration variances follow the same trends and are observed to decay more rapidly, particularly in regions close to the ceiling and at the left side of the room (occupied by the cylinder array) where negligible magnitudes were measured. The peak magnitudes of the $C_{peak}/\overline{C}$ ratio has shifted to originate from rows of cylinders closer to the source, with the region beyond $x/h_{exit,B}$ <-3 a scalar-free zone in which the scalar dye does not penetrate into, evidenced by negligible magnitudes of both $\overline{C}$ and $C_{peak}/\overline{C}$. These observations are similar to the effects of increasing the walking speed for room B previously observed in figure 3(c).

3.3. *Effects of human-to-source distance*

The effects of human-to-source distance for room A are presented in figure 6. As discussed in section 3.1, room A cylinders have an influence on the macro room flow while room B cylinders were only able to influence the local mean flow field due to the relative length-scales of the cylinders to the room. The mean velocity vectors presented in figure 6 show that the human-to-source distance has a very significant effect on the macro room flow. In fact, the mean flow patterns in the left side of the room can be observed to be completely different for all three test cases. Smaller but non-negligible differences can be observed at the right side of the room. This can be attributed to the relatively closer proximity to the outlet, which resulted in the mean flow being less affected by the motion of the cylinders. The A-HS1 test case, which has the cylinders closest to the source, appears to have the best scalar mixing properties along the direction of the motion (out-of-plane). This results in low magnitudes of mean concentrations observed in most regions of the room (figure 6(a)). The observation of non-uniform and anisotropic scalar mixing, yet again, indicate the need to consider more complex human motion for subsequent studies. Closer proximity to source does not necessarily always lead to better scalar mixing properties, as exemplified by the A-HS2 test case, which bucks this

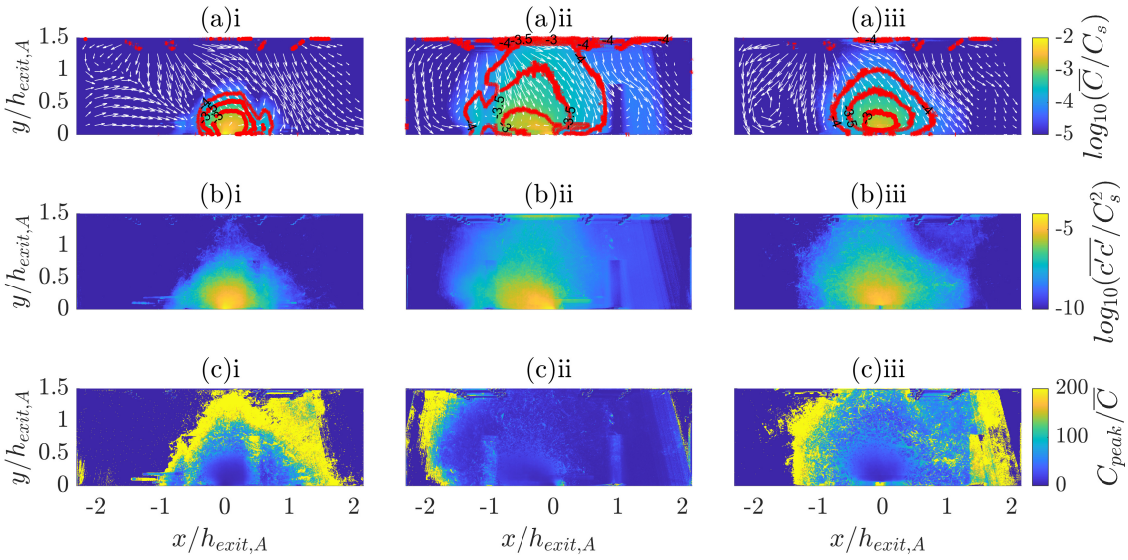

Figure 6. Effects of human-to-source distance, room A. (a) Mean concentration, (b) concentration variance and (c) peak-to-mean concentrations for test cases (i) A-HS1, (ii) A-HS2 and (iii) A-HS3 (i → iii: increasing human-to-source distance). The white arrows represent mean velocity vectors and red represents isocontour lines of the mean concentration.

trend (in comparison with A-HS1 and A-HS3), and has relatively high magnitudes of mean concentrations in most regions of the room. This is likely because of the non-linear interaction between the room flow and wake flow of the cylinders' which affects the scalar dispersion properties of all three test cases differently.

The concentration variance maps (figure 6(b)) follow similar patterns to the mean concentration, with peak magnitudes observed at the source and magnitudes decay with distance from source. These observations are consistent with the earlier results on the effects of walking speed and crowd density, and appears to be universal across the range of test cases investigated in this study. For the peak-to-mean concentration ratio (figure 6(c)), the A-HS2 test case shows completely different $C_{peak}/\overline{C}$ patterns to the other two test cases. Since this parameter is dependent on the mean flow field and intermittent scalar structures transporting high concentrations of dye, it is expected that the patterns will be very different if there are significant changes to the mean flow field of the room. We will discuss this in greater detail in the subsequent section.

3.4. Discussions on concentration PDFs

The concentration statistics previously presented in figures 3(c), 4(c), 5(c) and 6(c) showed interesting $C_{peak}/\overline{C}$ patterns. In particular, high magnitudes are observed to originate from rows of cylinders closer to the source with an increase in walking speed and crowd density for room B. To better understand the $C_{peak}/\overline{C}$ parameter, we consider the conditions where high magnitudes of $C_{peak}/\overline{C}$ are likely to occur. Due to the definition of $C_{peak}/\overline{C}$, low magnitudes of mean concentration is a necessary condition for high magnitudes of $C_{peak}/\overline{C}$ as shown in figures 3(c), 4(c), 5(c) and 6(c). However, high values of the concentration variance do not necessarily lead to high C_{peak} as shown in the results. As such, high magnitudes of $C_{peak}/\overline{C}$ should be expected only when the sampled location typically has very low concentrations, with a few rare instances where highly intermittent scalar structures transport high concentrations of dye to it.

Since the intermittency of the scalar structures affects the $C_{peak}/\overline{C}$ ratio, it would be useful to examine the PDF of the concentration. The concentration PDFs of B-WS3 test case sampled at 5 selected locations (see figure 3(c)iii) are presented in figure 7(a). Far from the source, the concentration values are almost always close to zero with only a couple of events out of the 1000 PLIF realization contributing to large concentration values (not visible in the plots). Close to the source, wider PDFs are observed which is consistent with the non-negligible mean concentration values

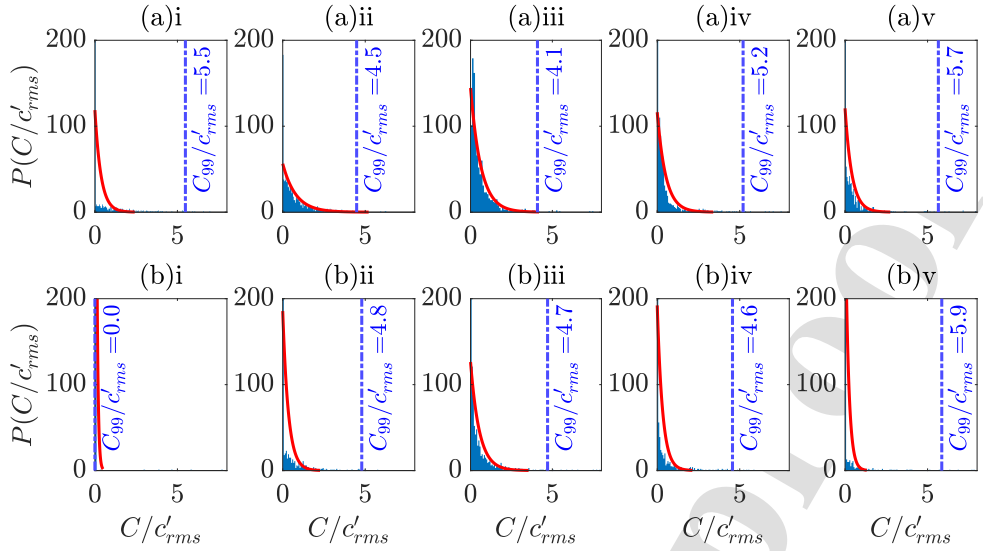

Figure 7. PDF for test case (a) B-WS3 (also equivalent to test case B-CD2) and (b) B-CD3 extracted at $y/h_{exit,C}$=1.14 and $x/h_{exit,C}$= (i) -3.03, (ii) -1.52, (iii) 0, (iv) 1.52 and (v) 3.03. Extracted locations are plotted as black dots on figures 3(c)iii and 5(c)iii. The red line shows an exponential fit.

observed in figure 3(a). The exponential function is a good fit to the PDF, which is consistent with the results observed for an empty room [29]. In the same plot, we have also appended the C_{99}/c'_{rms} ratio which is another parameter that can be used to determine exposures. This is defined as the ratio in which the concentration value is exceeded 1% of the time to the root-mean-square concentration fluctuations (i.e., exposure to a concentration of at least C_{99}/c'_{rms} for 1% of the time). This ratio generally ranges between 4.1 to 5.7 and does not appear to have a clear correlation with distance from source. The expected value for an exponential distribution at the 99% percentile can be derived as C_{99}/c'_{rms}=4.61 [29] which agrees well with the values here.

The PDFs associated with test case B-CD3 are presented in figure 7(b) (see figure 7(a) for PDFs of test case B-CD2). The general observations are similar to that of test case B-CD2. Wider PDFs are observed in the near-source region which indicates frequent scalar events that carry varying concentrations of dye to those locations, while far from the source where negligible mean concentration were measured, the PDFs showed concentrations values are almost always zero with only a few events contributing to high $C_{peak}/\overline{C}$ values. For most of the sampled locations, C_{99}/c'_{rms} ratio ranges between 4.6 to 5.9 but there is no clear correlation with the $C_{peak}/\overline{C}$ values or distance from source. Figure 7(b)i is a particularly interesting example that has high $C_{peak}/\overline{C}$ (see figure 5(c)iii) but zero C_{99}/c'_{rms} values, and can be attributed to the intermittent scalar events with high concentrations of dye occurring at less than 1% of the time in the 1000 PLIF realisations. This result shows that the use of both $C_{peak}/\overline{C}$ and C_{99}/c'_{rms} parameters are useful and provide different information for the purpose of determining exposures.

In figures 3(c), 4(c), 5(c) and 6(c), peak magnitudes of $C_{peak}/\overline{C}$ are observed to link the cylinders to the room ceiling. In particular, the increase in walking speed and crowd density for room B led to peak magnitudes shifting towards rows of cylinders closer to the source. This can be attributed to cylinder-generated turbulence that is more effective at expelling high concentrations of dye vertically out of the cylinder array and into the region of the room which typically has low dye concentrations. The dye is then entrained by large-scale structures of the length-scale of the room and advected to the room ceiling.

4. Concentration-velocity statistics and the scalar transport mechanisms

4.1. Effects of walking speed

To better understand the mean concentration patterns and underlying scalar transport mechanism, we examine the maps of the advective and turbulent scalar fluxes. The effects of walking speed for room B are presented in figure

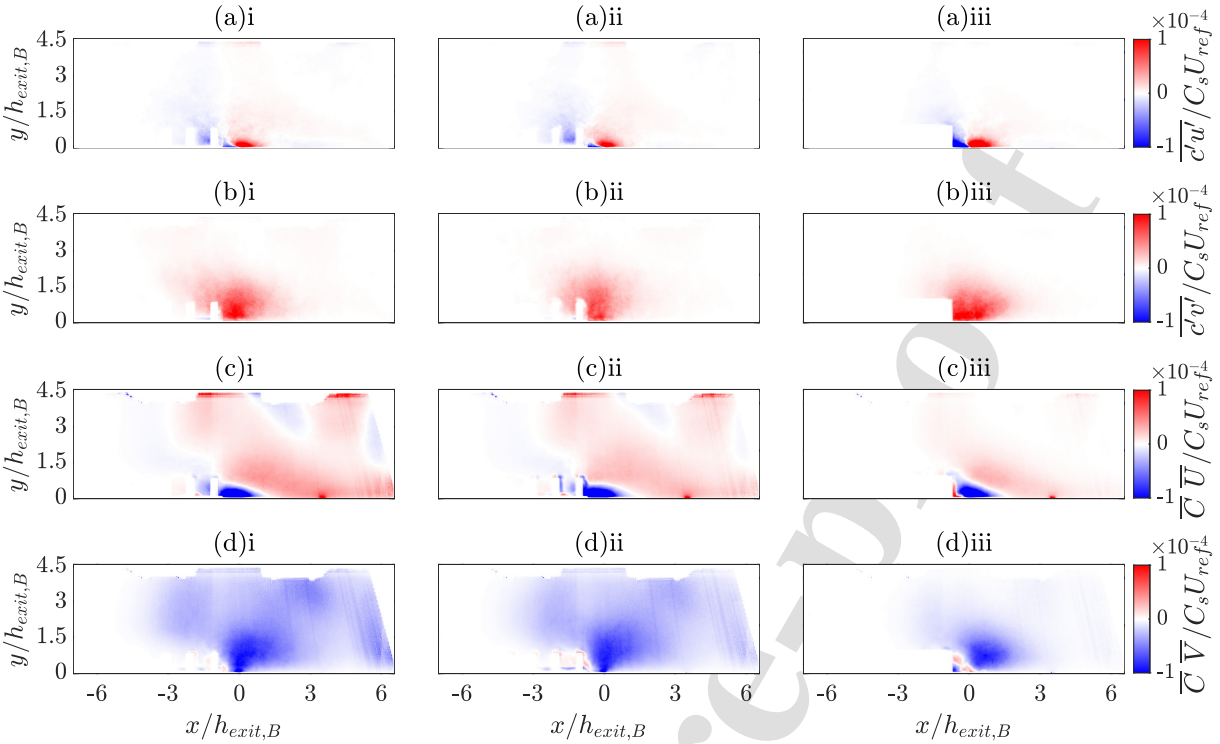

Figure 8. Effects of walking speed, room B. Mean (a) horizontal and (b) vertical turbulent scalar fluxes. Mean (c) horizontal and (d) vertical advective scalar fluxes. Test cases (i) B-WS0, (ii) B-WS1 and (iii) B-WS3 (i → iii: increasing walking speed).

8, where negative and positive values represent the directions of the fluxes relative to the tracer source at the origin. The magnitudes of the turbulent fluxes are highest at the source, decay rapidly with distance from source, and are negligible in regions far from the source. This can be attributed to the rapid decay of the concentration variance with distance from source (see figure 3(b)). The general patterns of the advective fluxes are similar, but they decay more slowly with increasing distance from source than the turbulent fluxes.

In the near-source region, the advective fluxes are of the same order of magnitude as the turbulent fluxes. As such, the scalar transport in the near-source region is dependent on the relative magnitudes and directions of the advective and turbulent fluxes. In particular, the vertical advective (downward) and turbulent (upward) fluxes are opposite in directions, which lead to a competing effect on whether the dye remains close to the ground. However, since the turbulent fluxes decay more rapidly with distance from source, and the vertical advective flux is downward in most regions of the room, the dye generally remains close to the ground. In the far-field, the advective fluxes dominate over the turbulent fluxes, and the scalar transport predominantly depends on the mean flow field of the room.

With an increase in walking speed, the magnitudes of the horizontal turbulent scalar flux at the near-source region increase, which suggests more rapid near-source turbulent scalar dispersion and greater turbulent entrainment of dye into the cylinder array. Dye is removed from the z=0 measurement plane due to the direction of the motion of the cylinder array, which is consistent with the observations of Marlow et al. [19] where they observed pollutant entrainment by the wake flow of the people. This leads to less dye being transported to the far-field and hence, lower magnitudes of the advective fluxes are observed in regions far from the source. Notably, low magnitudes of both advective and turbulent fluxes are observed in the left side of the room at higher walking speeds. This is consistent with low mean concentrations observed in this same region.

The scalar fluxes corresponding to the effects of walking speed for room A are presented in figure 9. Similar trends to room B are observed, with the turbulent scalar fluxes decaying more rapidly with distance from source and the advective fluxes dominant in regions far from the source. The increase in walking speed generally led to slightly higher magnitudes of the turbulent scalar fluxes at the near-source region, with the exception of the vertical turbulent

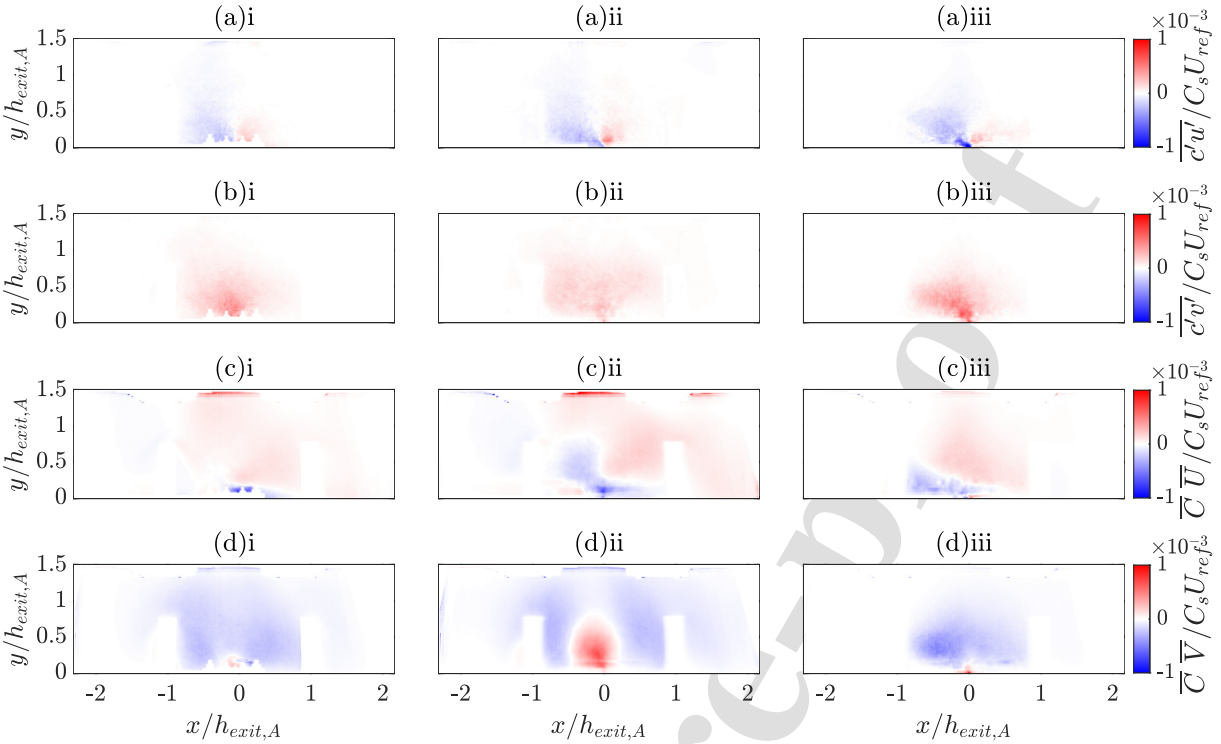

Figure 9. Effects of walking speed, room A. Mean (a) horizontal and (b) vertical turbulent scalar fluxes. Mean (c) horizontal and (d) vertical advective scalar fluxes. Test cases (i) A-WS0 baseline, (ii) A-WS1, (iii) A-WS3 (i → iii: increasing walking speed).

scalar flux for test case A-WS1, which has slightly lower magnitudes than the other two test cases (see figure 9b(ii)). This can be attributed to significant differences in the mean flow field, with test case A-WS1 observed to have mean upward flow close to the source (see velocity vectors in figure 4a(ii)), which is also captured as positive values of vertical advective scalar flux (see figure 9d(ii)).

For the advective scalar fluxes, the effect of higher walking speed generally led to more dye being advected towards the left cylinder, evidenced by greater magnitudes of the negative horizontal advective scalar flux for both A-WS1 and A-WS3 test cases relative to the baseline A-WS0 test case as shown in figure 9(c). At the highest walking speed (test case A-WS3), negligible magnitudes of the advective fluxes are observed beyond the cylinder positions (i.e., $x/h_{exit,B} < -1$ and $x/h_{exit,B} > 1$). Possibly, the increase in walking speed has led to more efficient dye entrainment by the cylinders' wake flow [19], with the dye subsequently being transported out of the measurement plane due to the direction of the cylinders' motion.

4.2. *Effects of crowd density*

To illustrate the effects of crowd density, the turbulent scalar fluxes for room B are presented in figures 10(a-b). Similar to the walking speed (room B) test cases previously presented in figure 8, the magnitudes of the turbulent fluxes here decay more rapidly with distance from source than the advective fluxes, resulting in the advective fluxes dominating scalar transport in regions far from the source. With an increase in the crowd density, the magnitudes of the turbulent scalar flux remain similar at the near-source region and decreases slightly for regions farther from the source.

The effect of increasing the crowd density is more significant for the advective fluxes as shown in figures 10(c-d). In the baseline B-CD0 test case, regions far from source show non-negligible magnitudes of the advective fluxes, which decrease to negligible values as the crowd density increases. Interestingly for the B-CD3 test case, the near-source advective flux pattern has changed significantly compared to the other two test cases, with positive magnitudes of the horizontal and vertical advective scalar fluxes observed close to the source. Although the length-scales of the

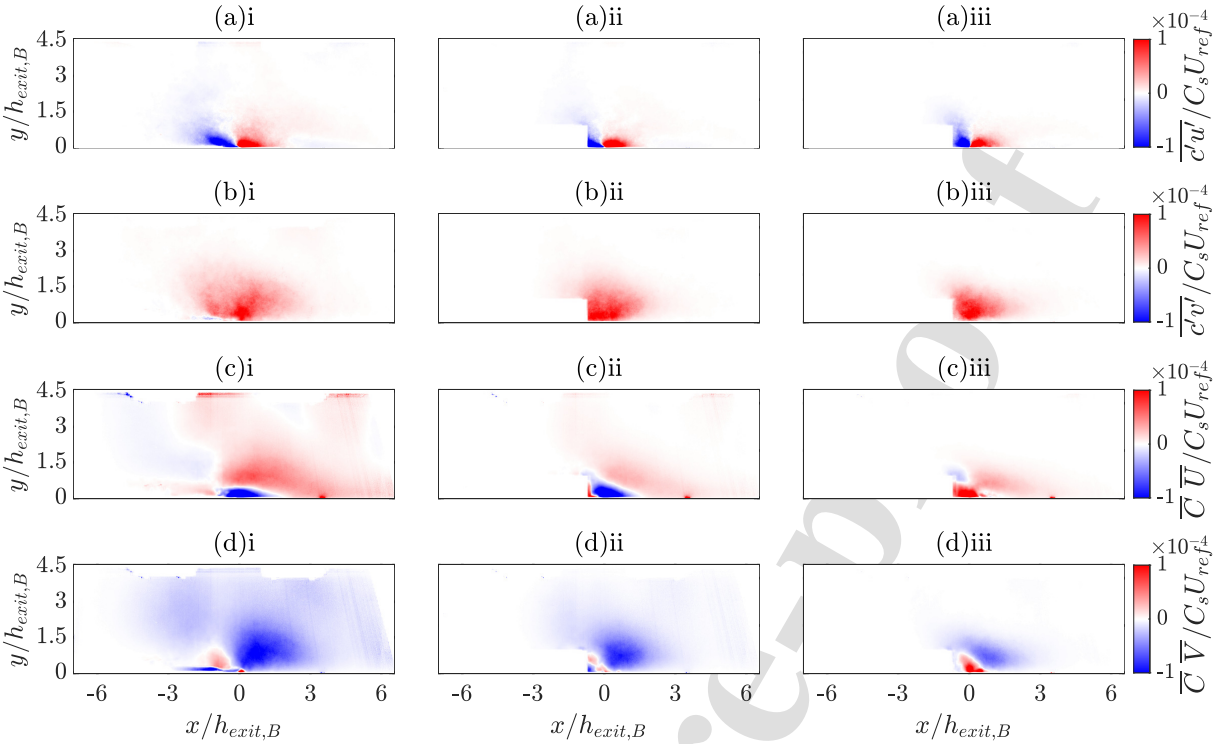

Figure 10. Effects of crowd density, room B. Mean (a) horizontal and (b) vertical turbulent scalar fluxes. Mean (c) horizontal and (d) vertical advective scalar fluxes. Test cases (i) B-CD0, (ii) B-CD2 and (iii) B-CD3 (i → iii: increasing crowd density).

cylinders are much smaller than that of the room and that their motion does not affect the macro room flow, this result shows it is still possible to induce changes to the near-source region which leads to changes in the advective fluxes. This is likely because of the relatively close proximity of the cylinders to the source. If the cylinders were farther from the source, the near-source advective flux patterns are not expected to be affected by the crowd density.

In addition, the more rapid decay of scalar fluxes with distance from source and negligible magnitudes of the mean concentration in the far field are similar to those on the effects of walking speed in room B (figures 5 and 8). This signifies more effective scalar mixing in the z-direction, which can be attributed to more rows of cylinders in the near-source region that are responsible for entraining the scalar dye out of the measurement plane and bringing in fresh ambient fluid.

4.3. Effects of human-to-source distance

The scalar fluxes corresponding to the effects of human-to-source position (in room A) are presented in figure 11. Although the variation of the human-to-source distance do not produce any significant trends, much larger differences are observed for the advective scalar fluxes compared to the turbulent scalar fluxes across the three test cases. This indicates that the advective scalar transport is the primary mechanism responsible for the changes in the mean concentration fields observed in figure 6(a). The fact that the cylinders can significantly influence the macro-scale flow and alter the flow field to the extent where trends in the scalar dispersion properties can no longer be observed, shows the human-to-source results discussed here are likely to be case specific. As such, if the length-scales of the people and the room are comparable (i.e. people in a room with 3 m ceiling), due care must be exercised when attempting to generalise the results to other applications.

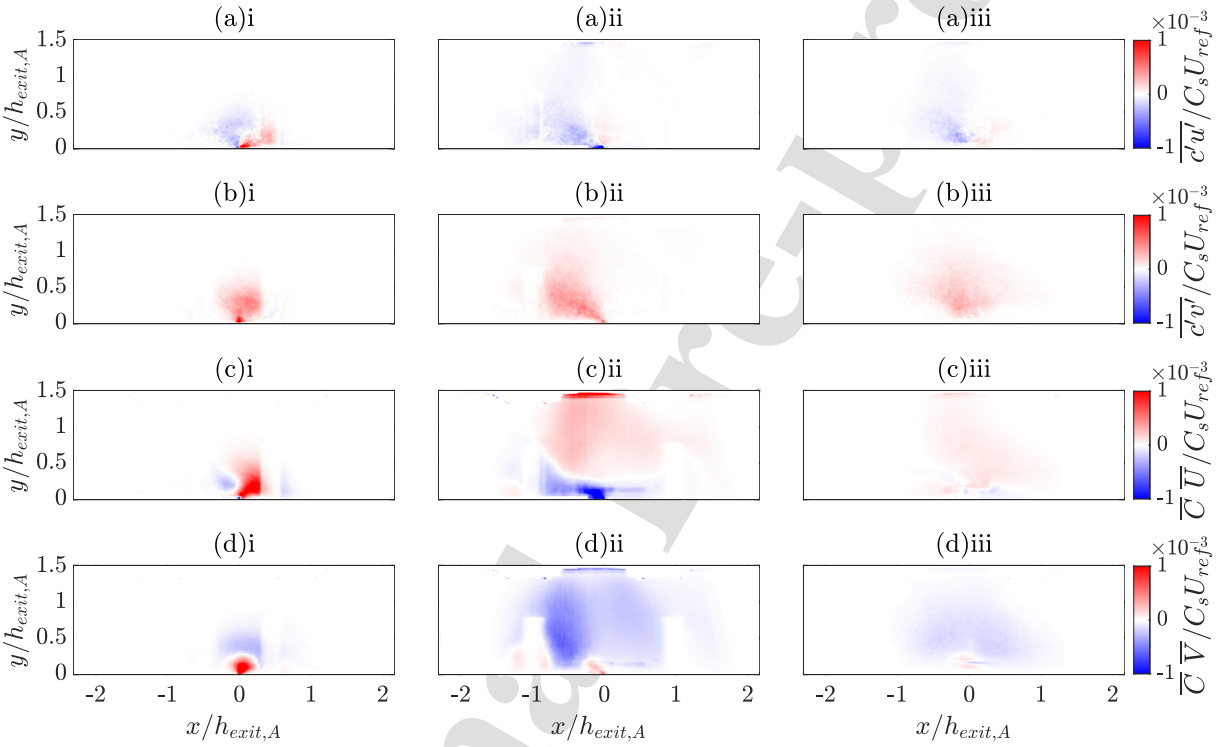

Figure 11. Effects of human-to-source distance, room A. Mean (a) horizontal and (b) vertical turbulent scalar fluxes. Mean (c) horizontal and (d) vertical advective scalar fluxes. Test cases (i) A-HS1, (ii) A-HS2 and (iii) A-HS3 (i → iii: increasing human-to-source distance).

5. Conclusions

In this study, the effects of walking speed, crowd density and human-to-source distance on the scalar dispersion of a passive point source in two scaled room models were experimentally investigated using simultaneous PIV and PLIF techniques in a water flume facility. For all test cases, the magnitudes of the mean concentration and concentration variance were observed to peak at the source and decay with distance from source. Low magnitudes of mean concentration were observed to be a necessary condition to achieve high magnitudes of peak-to-mean concentration ratios, together with instances of highly intermittent scalar structures transporting high concentrations of dye.

Room A, a 20:1 full-to-model scale model representing a 3 m ceiling room, showed that the macro flow field of the room is affected by the people's motion due to the comparable length-scales of the cylinders and the room. Varying the walking speed and human-to-source distance showed that the advective scalar fluxes undergo more significant differences than the turbulent scalar fluxes due to changes in the mean flow field. However, the lack of generic trends for the advective fluxes, and that their magnitudes are often comparable or even larger than the turbulent fluxes, indicate the scalar dispersion patterns for room A are likely to be case specific and cannot be generalised to other applications.

Room B, a 60:1 full-to-model scale model representing a 9 m ceiling room, showed the motion of the people only had a local influence on the flow field due to the relatively larger difference in length-scales of the cylinders and the room. The increase in walking speed and crowd density led to improved scalar mixing with the fresh ambient fluid particularly in the z-direction, evidenced by low mean concentrations in regions far from the source and higher magnitudes of the concentration gradient at the near-source region. The peak magnitudes of the peak-to-mean concentration ratio were observed to connect the cylinder arrays to the ceiling. With an increase in walking speed or crowd density, this region shifts to rows of cylinders closer to the source. This suggests high concentrations of dye that were swept into the cylinder array from the source are removed quicker due to the higher cylinder-generated turbulence, which were then entrained and removed by the large-scale structures in the room. This results in a larger scalar-free zone with less rows of cylinders exposed to high magnitudes of mean concentration and peak-to-mean concentration. Nonetheless, if the ventilation design, room geometry or source location changes, the flow field at the near-source region may change drastically (e.g. shifting the source location right beside the outlet can result in the dye being advected directly out of the room [29]), and hence these results may no longer be valid.

There are a few limitations of this study which we hope to address in the future. Firstly, the location and design of the ventilation inlets and outlets are expected to have a significant influence in the mean flow patterns of the room but were not considered in this study. Secondly, we have not considered the effects of buoyancy due to the thermal plume of the people, temperature differences at the room boundaries or other heat sources in the room. This is expected to be more significant in determining the room flow characteristics when there are low pressure variations within the room, and include scenarios where the crowd is stationary or when the ACH is low. Thirdly, the Reynolds number of the crowd motion was limited to $O(10^3)$ in this study. Although the turbulence regime of cylinder wake flows are expected to be similar up to $O(10^5)$, the results in this study have shown that the motion of cylinders can affect the macro room flow. In the context of indoor scalar dispersion, Re_{crowd} must be considered relative to the macro room flow characteristics, and a systematic study on the ratio of the Reynolds number of the room flow/inlet to the crowd motion would be helpful. Fourthly, the crowd motion was limited to two types of simplified movement in this study. This may not be representative of realistic scenarios and more complex crowd motion should be considered. Finally, the measurements of the turbulent diffusivity is an important aspect of this study that has many practical applications but has not been discussed. We hope to address these limitations in future studies.

The authors gratefully acknowledge the support of C.V.'s UKRI Future Leader's Fellowship (MR/S015566/1) and H.D.L.'s Royal Academy of Engineering Intelligence Community Postdoctoral Research Fellowship (ICRF2122-5-184).

The authors report no conflict of interest.

All the quantitative maps are made available in the University of Southampton data repository to enable comparison and validation with future research.

References

[1] Y. Li, G. M. Leung, J. W. Tang, X. Yang, C. Y. Chao, J. Z. Lin, J. W. Lu, P. V. Nielsen, J. Niu, H. Qian, A. C. Sleigh, H. J. Su, J. Sundell, T. W. Wong, P. L. Yuen, Role of ventilation in airborne transmission of infectious agents in the built environment-a multidisciplinary systematic review., Indoor Air 17 (1) (2007) 2–18.

[2] P. F. Linden, The fluid mechanics of natural ventilation, Annual Review of Fluid Mechanics 31 (1) (1999) 201–238.

[3] K. C. Cheng, V. Acevedo-Bolton, R. T. Jiang, N. E. Klepeis, W. R. Ott, O. B. Fringer, L. M. Hildemann, Modeling exposure close to air pollution sources in naturally ventilated residences: Association of turbulent diffusion coefficient with air change rate, Environmental Science & Technology 45 (9) (2011) 4016–4022.

[4] Y. Shao, S. Ramachandran, S. Arnold, G. Ramachandran, Turbulent eddy diffusion models in exposure assessment-determination of the eddy diffusion coefficient, Journal of Occupational and Environmental Hygiene 14 (3) (2017) 195–206.

[5] T. G. Foat, J. Drodge, J. Nally, S. T. Parker, A relationship for the diffusion coefficient in eddy diffusion based indoor dispersion modelling, Building and Environment 169 (2020) 106591.

[6] C. V. M. Vouriot, T. D. Higton, P. F. Linden, G. O. Hughes, M. van Reeuwijk, H. C. Burridge, Uniformly distributed floor sources of buoyancy can give rise to significant spatial inhomogeneities within rooms, Flow 3 (2023) E18.

[7] T. G. Foat, B. Higgins, C. Abbs, T. Maishman, S. Coldrick, A. Kelsey, M. J. Ivings, S. T. Parker, C. J. Noakes, Modeling the effect of temperature and relative humidity on exposure to sars-cov-2 in a mechanically ventilated room, Indoor Air 32 (11) (2022) e13146.

[8] H. C. Burridge, S. Bontitsopoulos, C. Brown, H. Carter, K. Roberts, C. V. M. Vouriot, D. Weston, M. Mon-Williams, N. Williams, C. J. Noakes, Variations in classroom ventilation during the covid-19 pandemic: Insights from monitoring 36 naturally ventilated classrooms in the uk during 2021, Journal of Building Engineering 63 (2023) 105459.

[9] H. Y. Kek, H. Tan, M. H. D. Othman, B. B. Nyakuma, P. S. Goh, S. L. Wong, X. Deng, P. C. Leng, A. S. Yatim, K. Y. Wong, Perspectives on human movement considerations in indoor airflow assessment: a comprehensive data-driven systematic review, Environmental Science and Pollution Research 30 (58) (2023) 121253–121268.

[10] S. Kinra, G. Lewendon, R. Nelder, N. Herriott, R. Mohan, M. Hort, S. Harrison, V. Murray, Evacuation decisions in a chemical air pollution incident: cross sectional survey, BMJ 330 (7506) (2005) 1471.

[11] J. Wang, T. T. Chow, Numerical investigation of influence of human walking on dispersion and deposition of expiratory droplets in airborne infection isolation room, Building and Environment 46 (10) (2011) 1993–2002.

[12] H. Tan, K. Y. Wong, M. H. D. Othman, B. B. Nyakuma, D. D. C. V. Sheng, H. Y. Kek, W. S. Ho, H. Hashim, M. C. Chiong, M. A. Zubir, et al., Does human movement-induced airflow elevate infection risk in burn patient's isolation ward? a validated dynamics numerical simulation approach, Energy and Buildings 283 (2023) 112810.

[13] N. Mingotti, R. Wood, C. J. Noakes, A. W. Woods, The mixing of airborne contaminants by the repeated passage of people along a corridor, Journal of Fluid Mechanics 903 (2020) A52.

[14] J. Hang, Y. Li, R. Jin, The influence of human walking on the flow and airborne transmission in a six-bed isolation room: Tracer gas simulation, Building and Environment 77 (2014) 119–134.

[15] L. Lv, Y. Wu, C. Cao, L. Zeng, J. Gao, W. Xie, J. Zhang, Impact of different human walking patterns on flow and contaminant dispersion in residential kitchens: Dynamic simulation study, in: Building Simulation, Springer, 2022, pp. 1–16.

[16] D. Al Assaad, K. Ghali, N. Ghaddar, Effect of flow disturbance induced by walking on the performance of personalized ventilation coupled with mixing ventilation, Building and Environment 160 (2019) 106217.

[17] Z. Liu, H. Liu, R. Rong, G. Cao, Effect of a circulating nurse walking on airflow and bacteria-carrying particles in the operating room: An experimental and numerical study, Building and Environment 186 (2020) 107315.

[18] Y. Zhao, Y. Feng, L. Ma, Impacts of human movement and ventilation mode on the indoor environment, droplet evaporation, and aerosol transmission risk at airport terminals, Building and Environment 224 (2022) 109527.

[19] F. Marlow, J. Jacob, P. Sagaut, A multidisciplinary model coupling lattice-boltzmann-based cfd and a social force model for the simulation of pollutant dispersion in evacuation situations, Building and Environment 205 (2021) 108212.

[20] J. Wu, J. Geng, M. Fu, W. Weng, Multi-person movement-induced airflow and the effects on virus-laden expiratory droplet dispersion in indoor environments, Indoor Air 32 (9) (2022) e13119.

[21] A. Hathway, I. Papakonstantis, A. Bruce-Konuah, W. Brevis, Experimental and modelling investigations of air exchange and infection transfer due to hinged-door motion in office and hospital settings, International Journal of Ventilation 14 (2) (2015) 127–140.

[22] H. M. Kamar, K. Y. Wong, N. Kamsah, The effects of medical staff turning movements on airflow distribution and particle concentration in an operating room, Journal of Building Performance Simulation 13 (6) (2020) 684–706.

[23] I. M. Abouelhamd, K. Kuga, S.-J. Yoo, K. Ito, Effect of crowd density, wind direction, and air temperature on the formation of individual human breathing zones in a semi-outdoor environment, Sustainable Cities and Society (2024) 105274.

[24] Y. Li, P. V. Nielsen, CFD and ventilation research, Indoor Air 21 (6) (2011) 442–453.

[25] P. V. Nielsen, Fifty years of cfd for room air distribution, Building and Environment 91 (2015) 78–90.

[26] J. D. Posner, C. R. Buchanan, D. Dunn-Rankin, Measurement and prediction of indoor air flow in a model room, Energy and Buildings 35 (5) (2003) 515–526. doi:https://doi.org/10.1016/S0378-7788(02)00163-9.
URL https://www.sciencedirect.com/science/article/pii/S0378778802001639

[27] C. Kandzia, D. Mueller, Flow structures and reynolds number effects in a simplified ventilated room experiment, International Journal of Ventilation 15 (1) (2016) 31–44.

[28] Z. J. Zhai, Z. Zhang, W. Zhang, Q. Chen, Evaluation of various turbulence models in predicting airflow and turbulence in enclosed environments by cfd: Part 1—summary of prevalent turbulence models, HVAC&R Research 13 (6) (2007) 853–870.

[29] H. D. Lim, T. G. Foat, S. T. Parker, C. Vanderwel, Experimental investigation of scalar dispersion in indoor spaces, Building and Environment 250 (2024) 111167.
[30] K. A. Bacik, B. S. Bacik, T. Rogers, Lane nucleation in complex active flows, Science 379 (6635) (2023) 923–928.
[31] C. Vanderwel, S. Tavoularis, Measurements of turbulent diffusion in uniformly sheared flow, Journal of Fluid Mechanics 754 (2014) 488–514.
[32] H. D. Lim, C. Vanderwel, Turbulent dispersion of a passive scalar in a smooth-wall turbulent boundary layer, Journal of Fluid Mechanics 969 (2023) A26. doi:10.1017/jfm.2023.562.
[33] C. H. K. Williamson, Vortex dynamics in the cylinder wake, Annual Review of Fluid Mechanics 28 (1) (1996) 477–539.
[34] T. L. Thatcher, D. J. Wilson, E. E. Wood, M. J. Craig, R. G. Sextro, Pollutant dispersion in a large indoor space: Part 1–scaled experiments using a water-filled model with occupants and furniture., Indoor Air 14 (4) (2004) 258–271.
[35] H. Abid, I. Baklouti, Z. Driss, J. Bessrour, Experimental and numerical investigation of the reynolds number effect on indoor airflow characteristics, Advances in Building Energy Research 14 (4) (2020) 424–449.
[36] J. Hou, Y. Sun, Q. Chen, R. Cheng, J. Liu, X. Shen, H. Tan, H. Yin, K. Huang, Y. Gao, X. Dai, L. Zhang, B. Liu, J. Sundell, Air change rates in urban chinese bedrooms, Indoor Air 29 (5) (2019) 828–839.
[37] W. F. Ten Berge, A. Zwart, L. M. Appelman, Concentration—time mortality response relationship of irritant and systemically acting vapours and gases, Journal of Hazardous Materials 13 (3) (1986) 301–309.
[38] T. L. Hilderman, S. E. Hrudey, D. J. Wilson, A model for effective toxic load from fluctuating gas concentrations, Journal of Hazardous Materials 64 (2) (1999) 115–134.

Highlights:

- Advective and turbulent scalar flux maps reveal underlying transport mechanism
- Crowd effects can induce non-uniform and anisotropic scalar mixing
- Scalar-free zone observed on the opposite side of the room from ventilation outlet
- Dispersion patterns in small rooms are case specific due to non-linear interactions

Declaration of interests

☐ The authors declare that they have no known competing financial interests or personal relationships that could have appeared to influence the work reported in this paper.

☒ The authors declare the following financial interests/personal relationships which may be considered as potential competing interests:

Christina Vanderwel reports financial support was provided by UK Research and Innovation. H.D. Lim reports financial support was provided by Royal Academy of Engineering.